inorganics

MDPI

Article

Synthesis of SiO_2/g-C_3N_4/Bi_2SiO_5@Bi_2O_3 Nanohybrid: A Bifunctional Catalyst for Hydrogen Generation and Antitumor Applications

Mohamed N. Goda *, Mohamed Khairy and Babiker Y. Abdulkhair *

Department of Chemistry, College of Science, Imam Mohammad Ibn Saud Islamic University (IMSIU), Riyadh 11623, Saudi Arabia; mkomran@imamu.edu.sa

* Correspondence: mnibrahim@imamu.edu.sa (M.N.G.); byabdulkhair@imamu.edu.sa (B.Y.A.)

Abstract

The fascinating features of nanomaterials have attracted immense interest across various fields, including nanoelectronics, magnetite-aided nanocatalysis, and nanomedicine. Herein, a 10% SiO_2/g-C_3N_4/Bi_2SiO_5@Bi_2O_3 triple nanohybrid was formulated via a simple protocol employing acacia powder as a capping/fuel agent. The XRD confirmed the presence of g-C_3N_4, Bi_2SiO_5, Bi_2O_3, and SiO_5 phases, and the TEM image shows densely packed, almost spherical nanoparticles of an average size of 9.2 nm. There was activity of the SiO_2/g-C_3N_4/Bi_2SiO_5@Bi_2O_3 in the field of hydrogen generation via $NaBH_4$ hydrolysis, and antitumor antiproliferation activity against HepG-2 and MCF-7 cells. The graphitized Bi_2O_3/SiO_2 exhibited HGRs of 303, 615, 785, and 1740 mL min^{-1} g^{-1} at 20, 30, 40, and 50 °C, respectively. Hydrolyzing $NaBH_4$ doses of 0.3, 0.5, 0.7, and 1.0 at 40 °C resulted in a dramatic evolution at HGRs of 526, 785, 1786, and 4000 mL min^{-1} g^{-1}, respectively. Furthermore, the g-C_3N_4/Bi_2O_3/SiO_2 antiproliferative effect against HepG-2 and MCF-7 cells showed a positive impact at 3.9 and 7.9 µg/mL, with IC_{50} values of 82.4 and 59.6 µg/mL, respectively. Moreover, the maximum dose of 500 µg/mL of SiO_2/g-C_3N_4/Bi_2SiO_5@Bi_2O_3 resulted in 93.8% inhibition of MCF-7 cells, whereas the same dose yielded 91.7% inhibition of HepG-2 cells. It is significant to note that, given the lower cost of SiO_2/g-C_3N_4/Bi_2SiO_5@Bi_2O_3 relative to currently prescribed antitumor medications, these outcomes can be considered ideal for practical use as antitumor agents.

Keywords: hydrogen energy; Bi_2SiO_5@Bi_2O_3; antitumor; hepatocellular; sustainability; breast cancer

Check for updates

Academic Editor: Antonino Gulino

Received: 6 May 2026
Revised: 19 June 2026
Accepted: 22 June 2026
Published: 24 June 2026

Copyright: © 2026 by the authors. Licensee MDPI, Basel, Switzerland. This article is an open access article distributed under the terms and conditions of the Creative Commons Attribution (CC BY) license.

1. Introduction

The fascinating features and practical applications of nanomaterials have garnered immense interest across various fields, including integrated catalysis, nanoelectronics, magnetite-aided nanocatalysis, and nanoelectrochemistry [1]. More desirable but difficult-to-achieve goals include developing innovative technologies for environmentally friendly, long-term, and cost-effective uses [2]. These nanomaterials have the potential to contribute to green chemistry by reducing waste, increasing reaction rates, improving atomic efficiency, and making catalyst recovery easier, in addition to meeting the conventional needs for catalysts that are selective for a specific catalytic reaction that converts raw materials into useful chemicals like fuels, water treatments, and pharmaceuticals. Although noble metal nanoparticles (NMPs) possess excellent catalytic properties, their high cost, tendency to self-aggregate, and limited abundance have driven demand for alternative catalysts [3]. The

rapid advancement of nanotechnology over the last few decades has given researchers a fresh perspective on traditional heterogeneous catalysts. Nanohybrids can now be routinely synthesized using various processes, including sol–gel [4], solvothermal, carbonization, electrodeposition, chemical vapor deposition, polycondensation, solid-state synthesis, and ball-milling [5–8]. The most prominent catalyst suitability features encompass environmental friendliness, economic feasibility, natural availability (as all or most of its constituents), and, of course, effectiveness for the intended application.

As one of the most abundant elements on Earth, the production of SiO_2 and SiO_2-based materials has garnered significant interest due to their cost-effectiveness [8]. Among SiO_2 forms, fumed silica (FUS, fluffy white powder) has widespread applications thanks to its characteristics, such as extremely low bulk density (20–2200 g L^{-1}) [9], high dispersibility, and a surface area of up to 400 m^2 g^{-1}. FUS is produced in industry by burning volatile silanes, such as silicon tetrachloride, in an oxygen–hydrogen flame. A wet FUS synthesis process may be based on reacting soluble silicates with acids, forming silica gels or precipitated silica, followed by flame pyrolysis of silanes, where the applied heat degree influences the FUS particle size and properties [10,11]. As reported in the literature, SiO_2 and its hybrids exhibit good performance in numerous applications, including photocatalytic degradation, glass and optical applications, energy storage, and hydrogen production [12,13].

Bismuth oxide, a semiconductor catalyst, exhibits six principal crystallographic polymorphs designated as α, β, γ, δ, ε, and ω, which correspond to the monoclinic, tetragonal, body-centered cubic (bcc), face-centered cubic, orthorhombic, and triclinic crystalline structures, respectively [14]. Bi_2O_3 possesses a low band gap, excellent stability, and high conductivity, while being devoid of hazardous elements, rendering it a favored option for photocatalytic applications. The α and β polymorphs have narrower band gaps, leading to greater light absorption and enhanced photocatalytic activity. The β polymorph is metastable, whereas the α polymorph is stable at ambient temperature, rendering α-Bi_2O_3 a viable photocatalyst for water splitting [15]. Notwithstanding its potential, the photocatalytic efficacy of pure Bi_2O_3 is considerably diminished by inadequate charge–carrier separation and rapid charge–carrier recombination. Bi_2O_3/SiO_2 has a wide range of applications, including photocatalytic dye degradation, radiation shielding, glass applications, energy storage, and optical applications [16–18]. A previous study on the hydrolysis of $NaBH_4$ on Bi_2O_3/SiO_2 reported notable H_2 production activity under milling conditions [19].

Carbon nanomaterials (CNMs: carbon nanotubes, nanofibers, nanoparticles, and carbon nitride) are known for their low cost, resistance to acidic and basic media, and the diversity of precursors, including industrial and agricultural wastes such as lemonwood, orange peels, onion shells, and potato peels [20,21]. C_3N_4 is an inexpensive two-dimensional synthetic polymeric CNM that is hard, lightweight, and possesses a large surface area, extraordinary stability (chemically and physically), and environmental friendliness [16,17]. Compared to regular CNMs, C_3N_4 offers several advantages, including unique structural and functional properties that make it well suited for biomedicine, photocatalysis, and energy storage. It is a unique, organic, metal-free semiconductor that operates in the visible range and can be tuned to adjust its electrical properties [22]. Its applications extend to various fields, including energy conversion, water purification, NOx decomposition, and the standardization of materials for identifying sites in oxidation reactions, as well as the development of H_2 and fuel cells [23,24]. Numerous studies have recommended doping with transition-metal oxides to enhance the properties of the resulting materials [25]. Doping can narrow the band gap, extend visible-light absorption, reduce electron–hole recombination, and expand surface area [26,27]. To improve C_3N_4's properties, recent

studies have focused on doping C_3N_4 with transition-metal/metalloid oxides, which has attracted significant attention [28]. Several studies suggest that incorporating transition metal oxides can enhance the properties and characteristics of base materials [25,29]. As a result, remarkable materials have found their way into various applications, including adsorption, photocatalysis, supercapacitance, anticancer activity, and hydrogen generation [30].

The rapid consumption of fossil fuel supplies, coupled with rising concentrations of harmful greenhouse gas emissions, has propelled the worldwide pursuit of alternative, renewable energy sources. Fossil fuels, including oil and coal, account for approximately 80% of the global energy supply, resulting in the depletion of natural resources and a persistent increase in atmospheric carbon dioxide levels, currently estimated at around 407.8 ppm [14]. Recently, green hydrogen production has emerged as a promising sustainable technology, specifically for its ability to reduce greenhouse gas emissions and alleviate the detrimental effects of climate change [31].

The World Health Organization stated that the majority of malignancies were attributable to environmental factors rather than hereditary causes, which might explain the current spread of cancer cases [32]. Several studies have demonstrated the efficacy of various bismuth- and C_3N_4-based nanomaterials as efficient antitumor and/or antibacterial agents [33,34]. The efficient interaction of nanoparticles results from their extensive surface area.

In this study, we designed a bifunctional nanocomposite, $Bi_2O_3/SiO_2/g\text{-}C_3N_4$, to determine how graphitization of the Bi_2O_3/SiO_2 system affects the catalytic production of H_2 from the hydrolysis of $NaBH_4$ and its anticancer activity. Due to the scarcity of published studies on the preparation and use of $Bi_2O_3/SiO_2/g\text{-}C_3N_4$ for hydrogen production, and its potential use as an anticancer agent, this study focused on the synthesis, characterization, and investigation of the catalytic properties and anticarcinogenic activity of this nanocomposite. Although the main objective of this work is to evaluate the catalytic performance of the synthesized composite for $NaBH_4$ hydrolysis, the antitumor assay is included as a complementary study to demonstrate the material's multifunctional potential. This additional section highlights that the same heterostructured system may also exhibit biological relevance, thereby broadening the practical significance of the proposed composite. Nevertheless, the catalytic behavior remains the central focus of this manuscript, and the biomedical results are presented as supporting evidence of the material's broader applicability.

2. Results and Discussion

2.1. XRD

The XRD of the Bi_2O_3/Silica@g-C_3N_4 nanocomposite is given in Figure 1. The XRD pattern shows the presence of a broad band centered at 21.93° related to the (100) plane of SiO_2 (Quartz) phase according to JCPDS Card 85–0335. The pattern also reveals strong broad bands at 12.565° and 27.565°, related to the (100) and (002) planes of the g-C_3N_4 phase, respectively. These planes are attributed to the in-plane repetition of the tri-striazine units and to the aromatic heterocyclic π-π interlayer stacking of graphitic carbon nitride, respectively [28]. The d-spacing of the (002) and (100) planes is 0.321 and 0.697 nm, respectively, corresponding to JCPDS card No. 87-1526 of g-C_3N_4 [32]. The XRD pattern shows several peaks attributed to the Bi_2O_3 phase, centered at 2θ = 27.82°, 32.86°, and 42°. In addition, 0°, 47.21°, 51.11°, 53.97°, 62.2° are related to (201), (220), (320), (400), (411), (203), and (431) planes of the tetragonal phase of Bi_2O_3 with space group P-421c according to card no 00-027-0050. On the other hand, the pattern shows peaks at 23.91°, 29.91°, and 56.87°, corresponding to (101), (103), and (213), which are characteristic of the Bi_2SiO_5 tetragonal phase according to card no 00-036-0288. The proportions of all observed phases

were determined to be 5, 15, 33, and 46% of SiO_2, g-C_3N_4, Bi_2SiO_5, and Bi_2O_3. These data confirm the formation of a heterostructure of SiO_2/g-C_3N_4/Bi_2SiO_5@Bi_2O_3 nanocomposite. The average crystallite size was calculated based on the observed peaks by the Scherrer equation [35]: $D_{XRD} = K\lambda/\beta\cos\theta$, where DXRD is the average size of nano-crystallites, K is the shape factor (typically, λ is the X-ray wavelength, β is the FWHM (Full-Width at Half-Maximum) in radians, and θ is the Bragg angle). The crystallite size was found to be 33.5 nm. The relative amounts of SiO_2, g-C_3N_4, Bi_2SiO_2, and Bi_2O_3 have a significant impact on the composite's catalytic performance. SiO_2 primarily serves as a support that enhances dispersion and structural stability, while g-C_3N_4 provides additional surface functionality and interfacial contact. The number of available active sites and the degree of interfacial synergies are determined by the percentage of the two primary active phases, Bi_2SiO_2 and Bi_2O_3. Because too little active phase lowers activity and too much loading may cause aggregation and reduced accessibility of active sites, an ideal phase ratio is necessary to maximize catalytic activity [16].

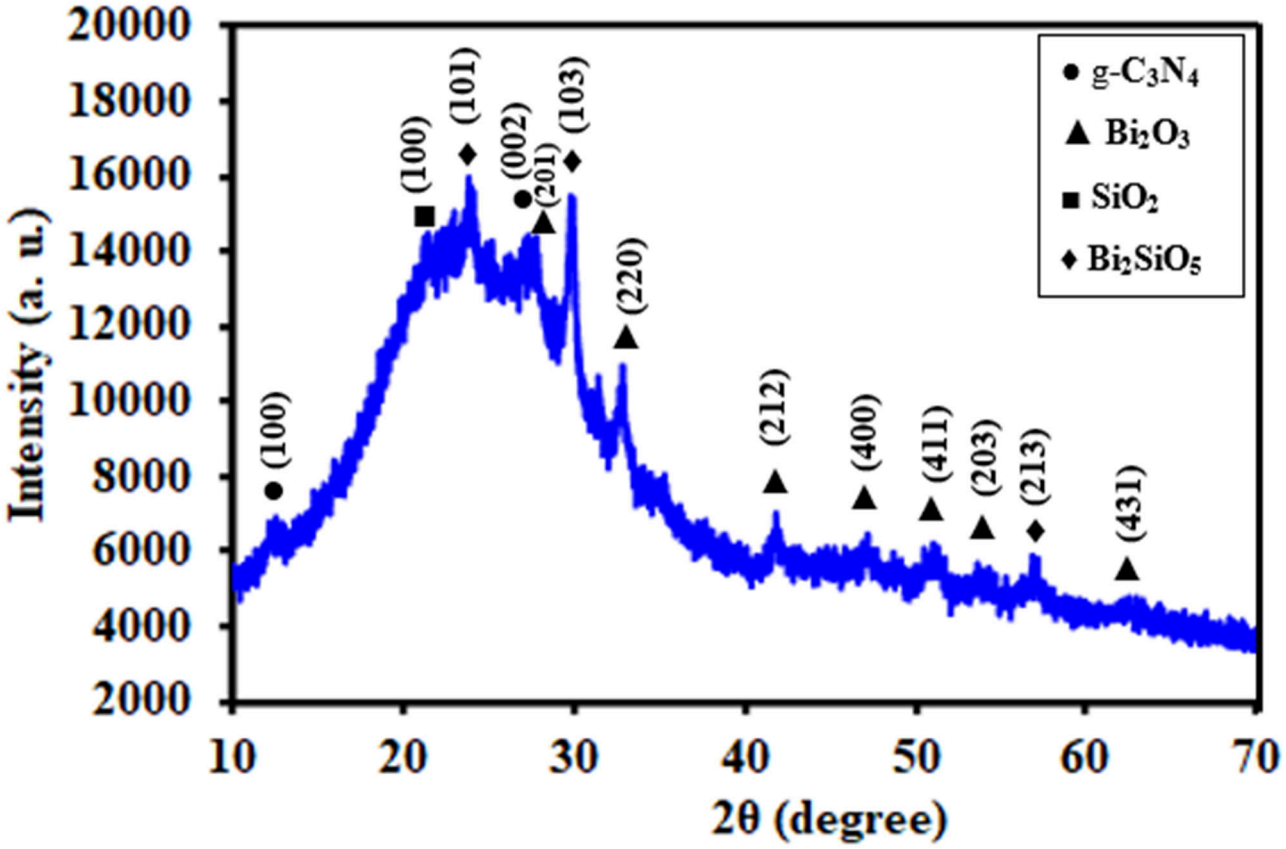

Figure 1. XRD pattern of SiO_2/g-C_3N_4/Bi_2SiO_5@Bi_2O_3 nanocomposite.

2.2. TEM Analysis

The TEM image and corresponding SAED pattern of SiO_2/g-C_3N_4/Bi_2SiO_5@Bi_2O_3 nanocomposite are given in Figure 2. The TEM image shows densely packed, almost spherical nanoparticles of an average size of 9.2 nm. These nanoparticles form a clearly agglomerated network. The image shows different contrast levels, indicating the presence of multiple components. The darker particles are due to the high-atomic-number Bi-based phases (Bi_2O_3 and Bi_2SiO_5), while the lighter, more transparent regions are due to amorphous SiO_2 and ultrathin g-C_3N_4 nanosheets. The diffuse, sheet-like features around the nanoparticles are important because they suggest that g-C_3N_4 acts as a supporting matrix, helping the particles spread out evenly and stopping them from growing too large. The close contact between these phases, without clear phase boundaries, indicates

that a well-defined heterojunction has formed, which is necessary for fast charge transfer between the two phases. In addition, the porous, loosely aggregated shape increases the available surface area and active sites, making it easier for reactants to adhere to the surface and improving catalytic efficiency. The TEM results strongly support the idea that a synergistic multi-component system has formed, with structural features well suited for high-performance catalytic applications. The corresponding selected area electron diffraction SAED of the composite displays a series of concentric diffraction rings, signifying the presence of polycrystalline domains with partial crystallographic orientation. The diffraction rings, from interior to exterior, are related to (220), (213), and (610), indexed to Bi_2O_3, Bi_2SiO_5, and Bi_2O_3, respectively. This indicates the successful creation of a heterostructured composite rather than a singular-phase material. The amorphous nature of SiO_2 makes the halo in the background appear diffuse. The weak diffraction from g-C_3N_4 suggests it has low crystallinity or a thin layered structure. This structural feature makes it easier for charge carriers to move and separate at heterojunction interfaces, which is an important factor in improving catalytic performance. The close connection between crystalline Bi_2SiO_5/Bi_2O_3 and the amorphous–semi-crystalline matrix (SiO_2/g-C_3N_4) also gives rise to many active sites. It makes it easier for electrons to move, which is important for increasing hydrogen production during $NaBH_4$ hydrolysis. In TEM analysis, the projected size is seen. Instead, the Scherrer equation calculates crystallite size from diffraction peak broadening over sample volume and averages coherent diffraction domains that contribute to XRD reflections. The Scherrer method proposes peak broadening due to finite crystallite size. Lattice strain, crystal flaws, experimental broadening, and overlapping diffraction peaks may underestimate it. Nanoparticles in nanohybrid systems form bigger crystalline aggregates that are coherent scattering domains in XRD but separate particles in TEM.

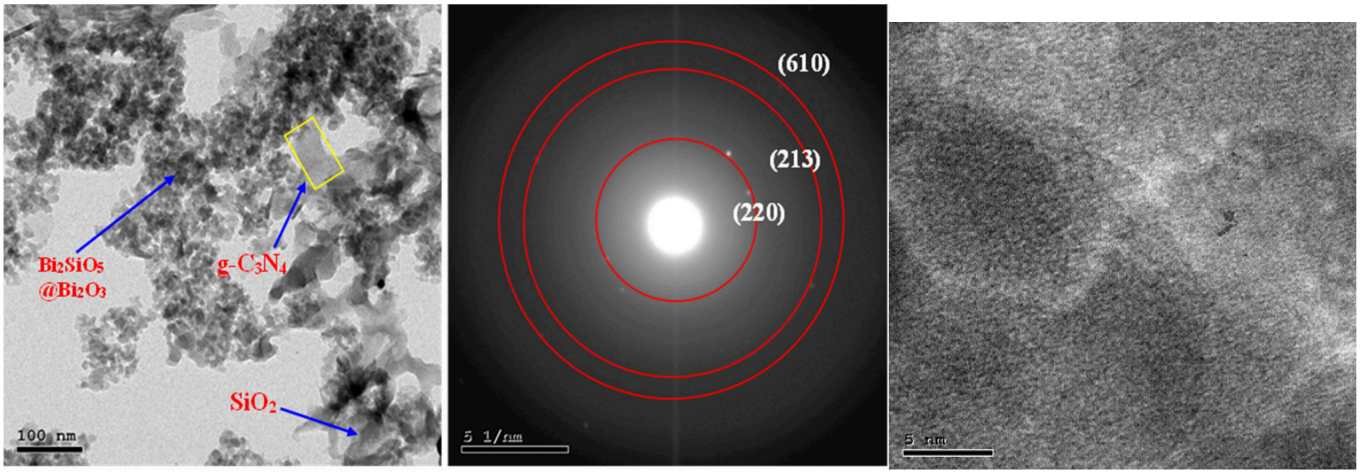

(**a**) (**b**) (**c**)

Figure 2. TEM image (**a**) and corresponding SAED pattern (**b**) and HRTEM image (**c**) of SiO_2/g-$C_3N_4/Bi_2SiO_5@Bi_2O_3$ nanocomposite.

2.3. XPS Analysis

The X-ray photon electron spectroscopy (XPS) survey of SiO_2/g-$C_3N_4/Bi_2SiO_5@Bi_2O_3$ nanocomposite and the deconvoluted XPS spectra of each element are given in Figure 3. The XPS survey of SiO_2/g-$C_3N_4/Bi_2SiO_5@Bi_2O_3$ nanocomposite exhibits several peaks related to Bi, Si, O, C, and N elements at binding energies of 30.08, 107.2, 537.71, 290.16, and 402.32 eV, respectively, indicating the high purity of the obtained catalyst and the formation of a heterostructure of SiO_2/g-$C_3N_4/Bi_2SiO_5@Bi_2O_3$ nanocomposite. The deconvoluted XPS spectra of the Bi element show two main peaks centered at 163.51 and 168.8 eV, corresponding to the Bi 4f7/2 and Bi 4f5/2 of the $[Bi_2O_2]^{2+}$ species, respectively, indicating

that the state of bismuth is Bi^{3+} [19,36,37]. The difference of 5.29 eV is associated with the spin–orbit splitting value for Bi_2O_3 (5.3 eV) [38]. The Si 2p spectra show two deconvoluted peaks at 101.52 and 102.83 eV, corresponding to Si-O-Si and Bi-O-Si, respectively, with a 1.31 eV separation [38]. The O 1s spectra of SiO_2 display three peaks at 528.6, 530.92, and 532.61 eV assigned to Bi-O-Bi, Si-O-Bi, and Si-O-Si [19,38,39]. The C 1s XPS spectra in Figure 3 display three deconvolution peaks at 282.76 eV related to the C-C bond, at 285.5 eV attributed to C=O bonding, and at 289.65 eV related to the sp2-hybridized C of N-C=N in g-C_3N_4 [40–42]. The N 1s spectra exhibit two main peaks at 399.49 eV and 402.16 eV, corresponding to C-N=C species and amino N (C-NH_x, x = 1, 2), respectively [43–48]. The XPS data demonstrate robust interfacial interactions among SiO_2, g-C_3N_4, and the bismuth-based phases. This close association may provoke interfacial charge redistribution and enhance electron movement across the heterostructure. In the composite, SiO_2 functions as a structural support, g-C_3N_4 establishes an electrically coupled interface, and the Bi-containing phases supply the active sites. This synergistic interface is anticipated to diminish charge–transfer resistance and enhance catalytic efficiency in $NaBH_4$ hydrolysis by facilitating more effective activation of the reactant at the catalyst surface.

2.4. Catalytic Generation of H_2

Sodium borohydride is regarded as an efficient chemical source of hydrogen owing to its high gravimetric hydrogen density and its capacity to release hydrogen in a controlled manner through hydrolysis [19,49]. During the reaction, sodium borohydride is hydrolyzed with water to produce sodium metaborate and hydrogen gas, as per the following equation: $NaBH_4 + 2H_2O \rightarrow NaBO_2 + 4H_2$. Despite the stability of $NaBH_4$ in alkaline media, its hydrolysis reaction is significantly accelerated in the presence of transition metal catalysts. Cobalt- and nickel-based catalysts are highly efficient at catalyzing hydrolysis, as they enhance the adsorption and interaction of hydride species and water molecules on the catalyst surface, thereby facilitating hydrogen release.

Previous investigation of $NaBH_4$ hydrolysis over Bi_2O_3/SiO_2 showed a remarkable activity toward the generation of H_2 under milled conditions [19]. In this investigation, we aimed to examine the impact of graphitization on the catalytic generation of H_2 from $NaBH_4$ hydrolysis in the Bi_2O_3/SiO_2 system. In our case, g-C_3N_4 can strengthen Bi_2O_3/SiO_2 catalysts for $NaBH_4$ hydrolysis by serving as a supportive, interactive matrix that disperses active particles, reduces aggregation, and enhances surface contact with reactants. Its nitrogen-rich framework can also modify the catalyst surface electronically, thereby promoting the adsorption and activation of water and borohydride species during hydrogen release [49]. As a result, incorporating g-C_3N_4 may enhance both catalytic efficiency and reusability in sodium borohydride-based hydrogen generation systems. The XPS results indicate strong interfacial interaction among SiO_2, g-C_3N_4, and the bismuth-based phases. This intimate coupling may induce interfacial charge redistribution and facilitate electron migration across the heterostructure. In the composite, SiO_2 acts as a structural support, g-C_3N_4 helps form an electronically coupled interface, and the Bi-containing phases provide the active sites. Such interfacial synergy is expected to reduce charge-transfer resistance and improve the catalytic performance in $NaBH_4$ hydrolysis by promoting more efficient activation of the reactant at the catalyst surface.

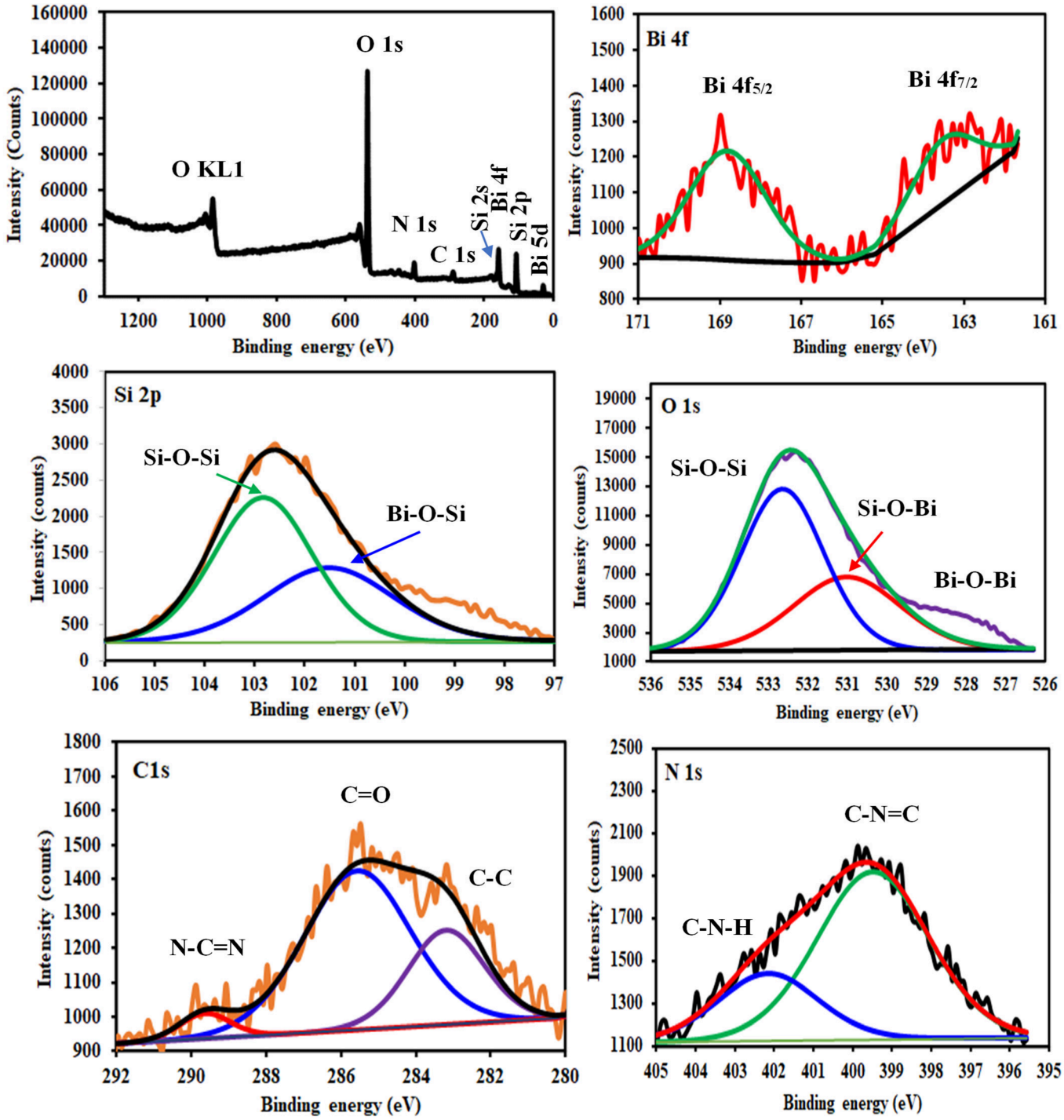

Figure 3. XPS survey of SiO_2/g-C_3N_4/Bi_2SiO_5@Bi_2O_3 nanocomposite, and deconvoluted XPS spectra of Bi 4f, Si 2p, O 1s, C 1s, and N 1s.

The catalytic hydrolysis of $NaBH_4$ over the graphitized Bi_2O_3/SiO_2 was studied under different reaction conditions, including the impact of reaction temperature and weight of $NaBH_4$, and the results are given in Figures 4–6. These catalytic runs were compared with the self-hydrolysis of $NaBH_4$ to illustrate the nanocomposite's catalytic activity. The effect of reaction temperature on the catalytic hydrolysis of $NaBH_4$ was examined under conditions of 0.02 g of catalyst and 0.5 g of $NaBH_4$ at a reaction temperature range of 20–50 °C, and the results are given in Figure 4a,b. An examination of the results presented in Figure 4a revealed two important points. Firstly, all of the catalytic runs exhibited activity higher than that of the self-hydrolysis, indicating the catalytic action of

the nanocomposite [19,49]. Secondly, as the reaction temperature increases, the reaction rate increases. The times required to liberate 70 mL of H_2 were 11.2, 5.6, 4.3, and 2 min at reaction temperatures of 20, 30, 40, and 50 °C, respectively. Values of HGR of 303-, 615-, 785-, and 1740 mL min^{-1} g^{-1} were obtained at reaction temperatures of 20, 30, 40, and 50 °C (Figure 4b). The relative amounts of SiO_2, g-C_3N_4, Bi_2SiO_2, and Bi_2O_3 have a significant impact on the composite's catalytic performance. SiO_2 mainly serves as a support that enhances dispersion and structural stability, while g-C_3N_4 offers extra surface functionality and interfacial contact. The number of available active sites and the degree of interfacial synergy are determined by the percentage of the two primary active phases, Bi_2SiO_2 and Bi_2O_3. Because too little active phase lowers activity and too much loading may cause aggregation and reduced accessibility of active sites, an ideal phase ratio is necessary to maximize catalytic activity [19]. Furthermore, two factors may account for the temperature dependence of $NaBH_4$ hydrolysis across all nanocomposites. First, according to transition-state theory, more molecules can overcome the activation energy barrier as temperature rises, since higher temperature increases the molecules' kinetic energy [49,50]. Second, higher heat activity increases the frequency of collisions between the reactants and the catalyst, thereby accelerating hydrogen generation [51,52].

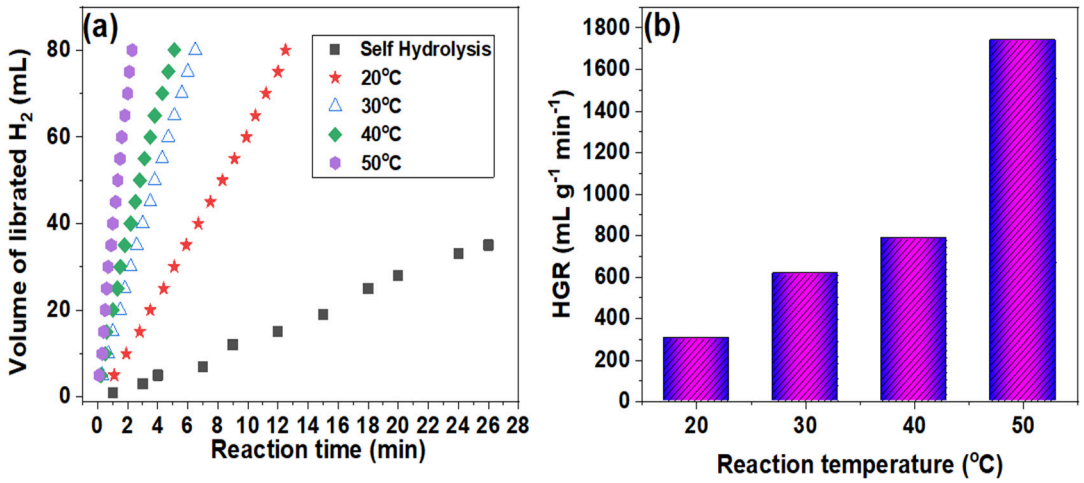

Figure 4. Variation in (**a**) volume of liberated H_2 with reaction time, and (**b**) HGR with reaction temperatures over g-C_3N_4/Bi_2O_3/SiO_2 ($NaBH_4$ = 0.5 g).

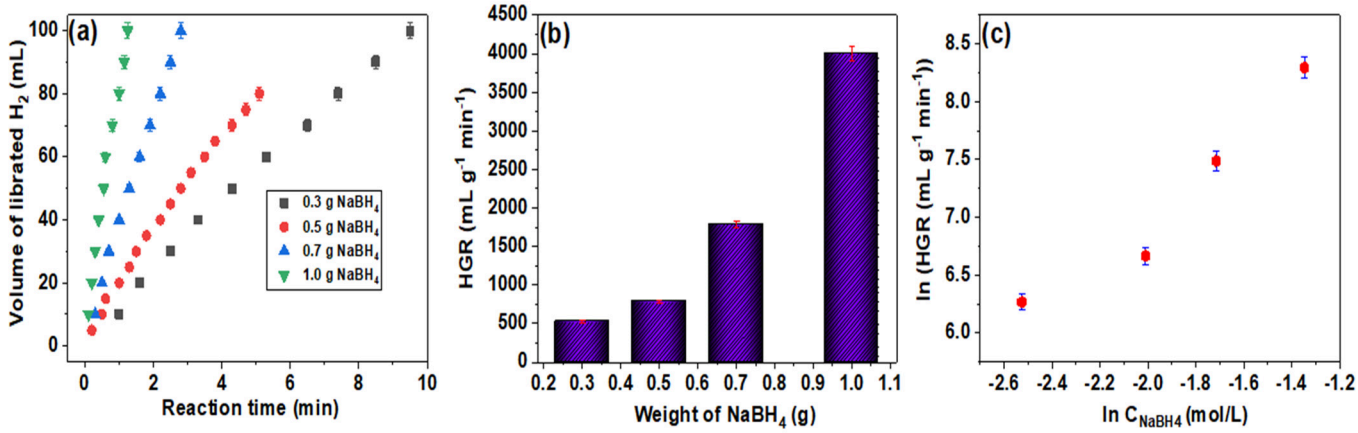

Figure 5. Variation in (**a**) volume of liberated H_2 with reaction time, (**b**) HGR with weight of $NaBH_4$, and (**c**) ln HGR vs. ln C_{NaBH4}, over g-C_3N_4/Bi_2O_3/SiO_2 catalyst at reaction temperature of 40 °C.

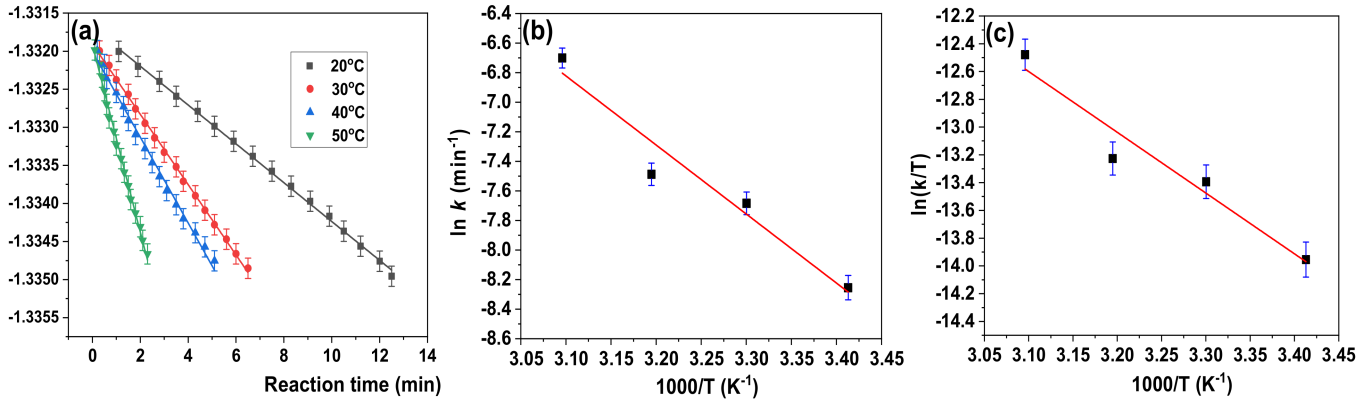

Figure 6. (**a**) Pseudo first order plot, (**b**) Arrhenius plot, and (**c**) Eyring plot for the catalytic hydrolysis of $NaBH_4$ over g-C_3N_4/Bi_2O_3/SiO_2 catalyst ($NaBH_4$ = 0.5 g).

Studying the influence of $NaBH_4$ dose on the catalytic hydrolysis of $NaBH_4$ is another important factor for managing and controlling hydrogen efficiency [19,49]. Figure 5a,b illustrates the catalytic hydrolysis reaction under different weights of $NaBH_4$ ranging from 0.3 g to 1.0 g at a reaction temperature of 40 °C. Close inspection indicates that, as the concentration of $NaBH_4$ in the reaction medium increases, the catalytic activity and, hence, the HGR value increase (Figure 5b). HGR values of 526, 785, 1786, and 4000 mL min^{-1} g^{-1} were obtained at $NaBH_4$ doses of 0.3, 0.5, 0.7, and 1.0, respectively. In fact, a dramatic evolution of HGR was observed. This enhancement resulted from the simultaneous increase in the concentrations of OH^- and BH_4^- in the reaction medium [19,53]. Moreover, the extent of adsorption of OH^- and BH_4^- on the active sites of the catalyst depends considerably on the concentration of $NaBH_4$ in the reaction medium [7]. The maximum catalytic performance is generally achieved when the adsorption of BH_4^- ions on the active sites is saturated at a certain weight percent of $NaBH_4$ in the reaction medium. At high concentrations, the excess OH^- and BH_4^- ions enhance the pH value of the medium, the viscosity of the medium, and the precipitation of $NaBO_2$, which covers the active sites of the catalyst, thus affecting the catalytic performance [54,55]. In the current study, the $NaBH_4$ concentrations are below those that lead to $NaBO_2$ pore blocking, suggesting that the enhancement in hydrogen generation rate remains due to concentration effects [52]. Additionally, this pattern implies that the reaction does not follow zero-order kinetics, as the hydrolysis rate over this catalyst is highly dependent on $NaBH_4$ concentration [56]. Plotting ln HGR against ln weight of $NaBH_4$ may also provide insight into the order of reaction (Figure 5c). The hydrolysis process is first-order with respect to $NaBH_4$, as shown in Figure 5c, yielding a straight line with a slope of 1.3 [49,57].

The reaction kinetics were further explored by treating the hydrolysis process as a pseudo-first-order system, assuming that the $NaBH_4$ concentration remains effectively constant relative to water and catalyst sites under the employed experimental conditions (Figure 6a). Linear plots of ln(a − x) versus time were obtained at 20, 30, 40, and 50 °C, with correlation coefficients of 0.9988, 0.9987, 0.9924, and 0.9940, respectively, indicating that the hydrogen generation profile fits well to a first-order dependence on the remaining reactant concentration over this temperature range (20–50 °C). The slope of each linear fit was taken as the apparent rate constant (k (min^{-1})) at the corresponding temperature, yielding values of 2.55×10^{-4}, 4.62×10^{-4}, 5.64×10^{-4}, and 12.3×10^{-4} min^{-1}. These rate constants were then used to construct an Arrhenius plot (Figure 6b), in which the natural logarithm of the rate constant was plotted against the inverse of absolute temperature (1/T). The linear regression of this plot allowed for the calculation of the activation energy (ΔE_a) from the slope, which was estimated to be 38.15 kJ mol^{-1}. This ΔE_a value falls within

the range typically reported for heterogeneous $NaBH_4$ hydrolysis over solid catalysts, suggesting that the reaction proceeds via a thermally activated surface process in which the rate-determining step is likely associated with the adsorption or activation of borohydride species at the catalyst–solution interface. However, this value of activation energy is comparable with that of cobalt/colloidal carbon sphere (33.4 kJ mol^{-1}) [58] and Co/3D graphene oxide (37 kJ mol^{-1}) [59], while still lower than that of other catalytic systems including Ru /$LiCoO_2$ (68.5 kJ mol^{-1}) [60], Bi_2O_3/SiO (69.25 kJ mol^{-1}) [19], NiB/$NiFe_2O_4$ (72.52 kJ mol^{-1}) [61], Mn_2O_3@C (41.55 kJ mol^{-1}) [49], Co/IR-120 (66.7 kJ mol^{-1}) [62], $MoO_3/MgAl_2O_4$ (47.55 kJ mol^{-1}), Pd/ZIF-67 (58.5 kJ mol^{-1}) [58] $CuO/MgAl_2O_4$ (41.45 kJ mol^{-1}) [7]. The thermodynamic parameters for the hydrolysis reaction were further examined using the Eyring equation with the temperature-dependent rate constants, as shown in Figure 6c. This analysis yielded an activation enthalpy ($\Delta H^{\#}$) of 36.1 J mol^{-1} and an activation entropy ($\Delta S^{\#}$) of −171.3 J mol^{-1} K^{-1}. The positive value of $\Delta H^{\#}$ indicates that the formation of the transition state is an endothermic process, requiring energy to be overcome to proceed with the rate-determining step [7]. On the other hand, the negative value of $\Delta S^{\#}$ indicates that the activated complex is more ordered than the reactants, suggesting that the transition state is structured with stronger binding or interaction between the BH_4^- and water molecules on the catalyst surface [7]. As one of the most important industrial features of catalysts, the reusability of the current catalyst was studied and the results included in Figure 7a,b. HGR values of 785, 770, 714, and 660 mL min^{-1} g^{-1} were respectively obtained after zero, one, two, and three cycles of use. These results revealed that the catalyst could be recycled three times with almost the same values of HGR, indicating the good reusability of the catalyst under investigation. Furthermore, the stability of $Bi_2O_3/SiO_2/g\text{-}C_3N_4$ was tested by comparing the FTIR of the as-prepared nanohybrid with that of regenerated catalyst (Figure 7c). Both $Bi_2O_3/SiO_2/g\text{-}C_3N_4$ batches showed identical peaks match except for the broadening of the OH-stretching vibration band (3200–3550 cm^{-1}) in the regenerated $Bi_2O_3/SiO_2/g\text{-}C_3N_4$ batch, which is allocatable to absorbed moisture and/or formation of trace metal hydroxide.

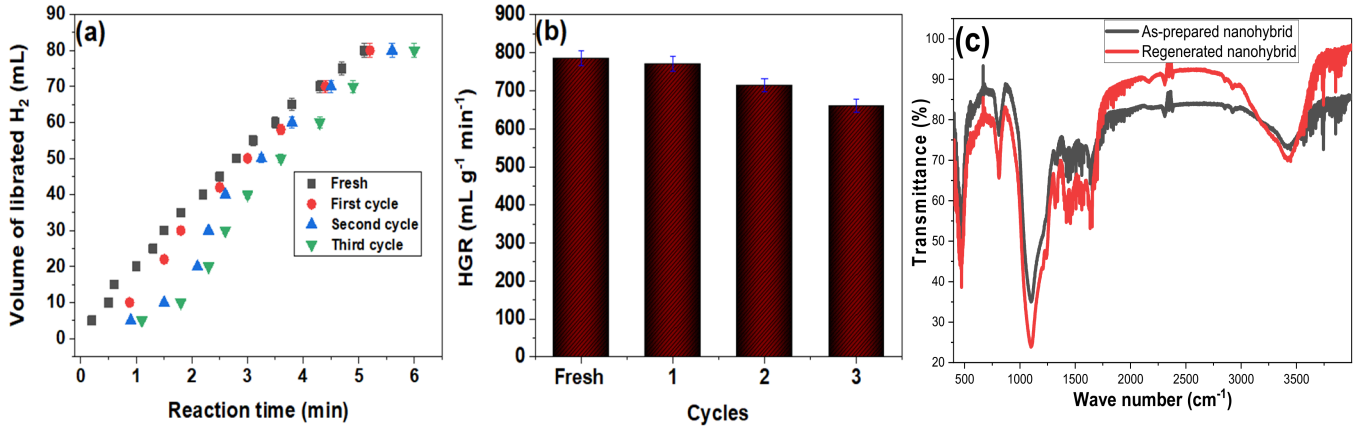

Figure 7. Variation in (**a**) volume of liberated H_2 with reaction time, (**b**) HGR with the number of cycles over g-C_3N_4/Bi_2O_3/SiO_2 catalyst at a reaction temperature of 40 °C ($NaBH_4$ = 0.5 g), and (**c**) FTIR analysis of the as-synthesized $Bi_2O_3/SiO_2/g\text{-}C_3N_4$ and the regenerated batch.

A comparison of the catalytic activity of the $Bi_2O_3/SiO_2/g\text{-}C_3N_4$ nanocomposite with the previously reported catalysts in the catalytic hydrolysis of $NaBH_4$ is shown in Table 1. The catalytic activity of the present catalyst is found to be better than that of previously reported catalysts, with higher hydrogen generation rates (HGRs) of 303, 615, 785, and 1740 mL min^{-1} g^{-1} at 20, 30, 40, and 50 °C, respectively, with 0.5 g of $NaBH_4$. Moreover, the present catalyst exhibits a high HGR of 4000 mL min^{-1} g^{-1} at 40 °C with 1.0 g of $NaBH_4$.

Compared with the Co-based catalysts, the present catalyst shows a better HGR than the CoB/SBA-15 catalyst (636.6 mL min^{-1} g^{-1} at 60 °C) [63] and the CoB/ZIF-8 catalyst (506 mL min^{-1} g^{-1} at 35 °C) [64] at lower temperatures and without the use of a promoter like NaOH. Moreover, the activation energy of the present catalyst (38.1 kJ mol^{-1}) is lower than the activation energy of the CoB catalysts (56.6 kJ mol^{-1} for Co–B/Na-bentonite [57] and 72.66 kJ mol^{-1} for Ni_1Co_3/activated carbon [65]). The synergistic effect of g–C_3N_4 in enhancing reactant accessibility and active-site dispersion within the Bi_2O_3/SiO_2 framework is responsible for this improved performance, positioning the current material as a highly competitive, non-noble-metal catalyst for practical hydrogen generation.

Table 1. Comparison of the catalytic performance of the current catalyst with that previously reported in the literature.

Catalyst	Reaction Temperature (°C)	Reaction Conditions	HGR (mL min^{-1} g^{-1})	ΔE_a (kJ mol^{-1})	Reference
Co–B/Na-Bentonite	50	5% $NaBH_4$, 10% NaOH	1602	56.6	[55]
Co–B/Bentonite			921.94	55.76	
Co-Ni/Magnetic bentonite	30	5 wt% $NaBH_4$ and x wt% NaOH	186	44.98	[65]
Cu-Asp MOF	40	0.189 g (0.05 mol/L) $NaBH_4$	186.5	42.7	[56]
Co@SiO_2 xerogel	45	1 wt% NaOH + 1 wt% $NaBH_4$	133.7	15.2	[66]
CoO/CaO (Egg Shell)	30	1 wt% $NaBH_4$ +1 wt% NaOH	432	16.78	[67]
CoB/SBA-15	60	0.4 g $NaBH_4$	636.6	49.8	[62]
9% Co/Al_2O_3	30	5 wt% $NaBH_4$ + 10 wt% NaOH	220	45.64	[68]
Ni_1Co_3/Activated Carbon	30	5 wt% $NaBH_4$ + 5 wt% NaOH	252	72.66	[64]
CoB/ZIF-8	35	1.67 wt% $NaBH_4$, 5 wt% NaOH	506	57.72	[63]
Fe/$Fe_2(MoO_4)_3$	100	$NaBH_4$ (5.3 mM)	1057	21.11	[69]
Ni-B	60	20 wt%$NaBH_4$, 5 wt% NaOH	130.0	61.8	[70]
MOF-derived Co@C	30	2 wt% $NaBH_4$, 2 wt% NaOH	267	56.9	[71]
Bi_2O_3/SiO_2/g-C_3N_4	20	0.5 g $NaBH_4$	303	38.1	Current work
	30		615		
	40		785		
	50		1740		
	40	1.0 g $NaBH_4$	4000		

2.5. Mechanism of $NaBH_4$

$NaBH_4$ catalytic hydrolysis over BiO_3/SiO_2/g-C_3N_4 most likely follows a four-stage process that is comparable to previously described processes [72,73]. Initially, in solution, BH_4^- ions separate from $NaBH_4$ and chemisorb onto electron-deficient Bi^{3+} sites in the Bi_2O_3 phase. Adsorbed H^- ion and BH_3^- fragments are created when hydride species (H^-) move to adjacent Bi^{3+} or Si^+ surface sites, weakening the B–H bonds. H^- and H_2O combine to make H_2, OH^-, and BH_3; and (iv) OH^- ion interacts with BH_3 to form $BH_3(OH)$ intermediate. This cycle produces $B(OH)_4$ and releases hydrogen molecules until all hydrogen atoms are swapped for hydroxyl ions. At these interfaces, g-C_3N_4 enhances local polarity and reactant interaction. The $BH_3(OH)$ species is then gradually consumed in three additional hydrolysis cycles, yielding three additional H_2 molecules and $NaBO_2 \cdot H_2O$ as the final product. The two reactants, BH_4^- and H_2O, were previously known to adsorb on two different active metal species, Bi^{3+}, Si^{4+}; Zn^{2+}, Cd^{2+} [19,49], or the same metal with different electronic structures, Cu^{2+}, Cu^+; Co^{2+}, Co^{3+}; and Mn^{3+}, Mn^{4+} [6,52,72–75].

In our case, different Bi^{3+} and Si^{+4} couples (as electron-deficient sites) may be involved in the adsorption of BH_4^- and H_2O, or mixed Bi oxidation states (Bi^{3+}/Bi^{+5}). In addition, the N-sites in g-C_3N_4 may act as electron-rich sites. The XPS discovery of Bi, Si, and lattice oxygen confirms a Michaelis–Menten route dominated by BH_4^- binding to Bi^{3+}. A Langmuir–Hinshelwood pathway is also possible, where sequential H_2 evolution (one H_2O per hydride) is driven by the co-adsorption of both reactants at Bi_2O_3/g-C_3N_4 borders. Through coordination and electron donation, the nitrogen-rich g-C_3N_4 matrix stabilizes these sites, allowing for high activity without the need for precious metals.

2.6. HepG-2 and MCF-7 Antiproliferation by g-C_3N_4/Bi_2O_3/SiO_2

The antitumor activities of the Bi_2O_3/SiO_2/g-C_3N_4 nanohybrid against HepG-2 and MCF-7 were evaluated (Figure 8). The Bi_2O_3/SiO_2/g-C_3N_4 showed 3.9 and 7.9 µg/mL as its lowest effective doses in treating HepG-2 and MCF-7 cells, respectively. The Bi_2O_3/SiO_2/g-C_3N_4 showed IC_{50} values of 82.4 and 59.6 µg/mL for MCF-7 and HepG-2 cells, respectively (Figure 4a,b). Moreover, the maximum dose of 500 µg/mL of Bi_2O_3/SiO_2/g-C_3N_4 demonstrated 93.8% inhibition of MCF-7 cells, while the same dose resulted in 91.7% inhibition of HepG-2 cells. The antiproliferative efficacy of Bi_2O_3/SiO_2/g-C_3N_4 is ascribed to the chemical stability and high surface area of the g-C_3N_4 matrix, which promotes electron transfer. At the same time, the transition metal oxide (Bi_2O_3) may induce reactive oxygen species, resulting in lipid peroxidation in MCF-7 and HepG-2 cells [76]. The heterojunction structure of Bi_2O_3/SiO_2/g-C_3N_4 may improve electron–hole separation, thereby reducing charge recombination and promoting reactive oxygen generation [77]. The Bi_2O_3/SiO_2/g-C_3N_4 nanohybrid exhibited remarkable efficacy against MCF-7 and HepG-2 cell lines. The g-C_3N_4-based nanohybrids diminish tumor cell viability by generating reactive oxygen species, elevating oxidative stress, impairing mitochondrial function, and triggering apoptosis [76]. On the other hand, Bi_2O_3 nanoparticles exert toxic effects by compromising cellular antioxidant defenses, including Bi_2O_3-induced reactive oxygen species (ROS) generation, glutathione depletion, caspase-3 activation, and cell-cycle arrest in HepG-2 cells [77–80]. The anticancer efficacy of Bi_2O_3/SiO_2/g-C_3N_4 likely involves reactive oxygen species-mediated oxidative stress, subsequently triggering apoptotic pathways. Given its relatively low cost compared to currently prescribed antitumor medications, additional in vivo investigations and, ideally, practical use as antitumor agents are required.

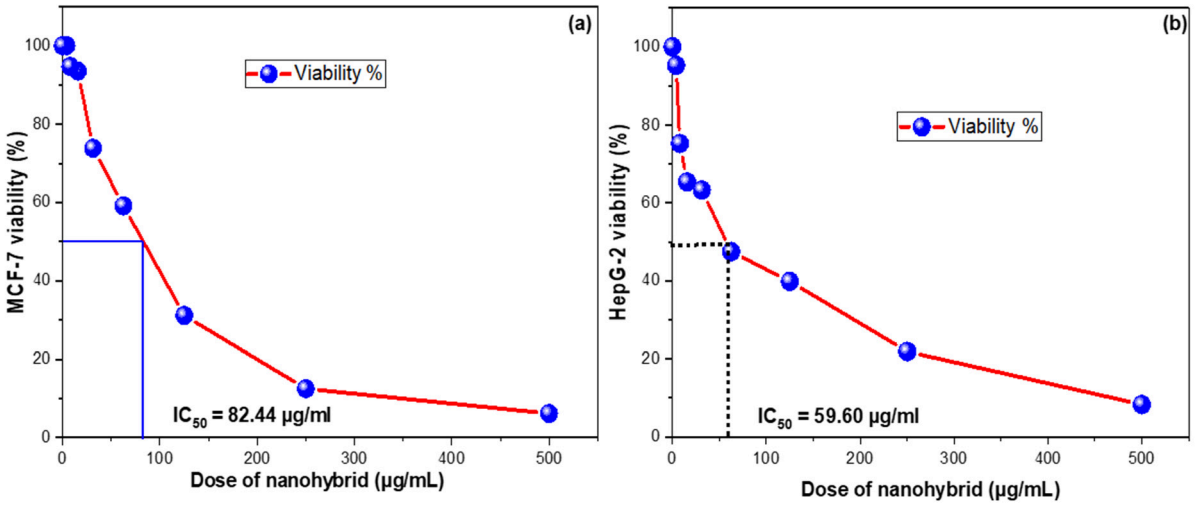

Figure 8. The antiproliferative efficacy of Bi_2O_3/SiO_2/g-C_3N_4 against the cell viability of (**a**) MCF-7 and (**b**) HepG-2 cells.

3. Materials and Methods

3.1. Materials

Bismuth nitrate ($Bi(NO_3)_3 \cdot 5H_2O$, 99%) was procured from BDH, Köln Bonn, Germany. Hydrophilic fumed silica (SiO_2, 99%) was acquired from HIFULL Yichang, Yiling, China. Acacia powder (AcP) and sodium borohydride ($NaBH_4$, 98%) were obtained from Fluka, Buchs, Switzerland. Urea (98.5%) and ethylene glycol (ETG, 99%) were acquired from Sharlau, Barcelona, Spain. Fetal bovine serum, L-glutamine, gentamicin, and Trypsin-EDTA were acquired from Lonza, Bornem, Belgium. The human hepatocellular and human breast cancer cell lines (HepG-2 and MCF-7) were procured from ATCC (Rockville, MD, USA). Dimethyl sulfoxide (DMS), tetrazolium dye, and trypan blue dye were acquired from Sigma-Aldrich, Miami, FL, USA. Deionized water (MQW) MilliQ, Seattle, WA, USA was employed for all preparations.

3.2. Preparation of g-C_3N_4/Bi_2O_3/SiO_2

A mass of 4.0 g of SiO_2, an amount of $Bi(NO_3).5H_2O$ appropriate to produce 0.5 g of Bi_2O_3, 1.0 g of AcP, and 10 mL of ETG were placed in a ball milling crucible. The machine was operated at 400 RPM for twenty minutes. The content was transferred quantitatively using deionized water (20 mL) to a porcelain dish and placed in an oven set at 250 °C to remove the ETG gradually without causing splashing. In the pre-calcination treatment, AcP expanded between Bi^{3+}/SiO_2, creating polymeric boundary walls between the ions. The porcelain dish was calcined at 650 °C for 4.0 h, during which AcP served as both a fuel and a capping agent, inhibiting the agglomeration of newly produced particles and preventing their further expansion by crystal growth extension. The product was cooled to room temperature, and the appropriate amount of urea to produce 0.5 g of g-C_3N_4 was ground with the Bi_2O_3/SiO_2 product. The triple mixture was transferred to a 50 mL porcelain crucible, covered with its lid wrapped with aluminum foil to prevent oxygen, and heated at 550 °C for 2.0 h to produce the Bi_2O_3/SiO_2/g-C_3N_4.

3.3. Characterizations

The synthesized *g*-C_3N_4/Bi_2O_3/SiO_2 nanocatalyst was analyzed using X-ray diffractometry (Bruker, Miami, FL, USA), surface area analysis (ASAP-2020, Micromeritics, Miami, FL, USA), transmission electron microscopy (JEM-1400, JEOL, Pleasanton, CA, USA), and scanning electron–energy-dispersive X-ray spectroscopy (SEM-EDX, JSM-IT500HR, JEOL, USA). A KRATOS-AXIS DLD spectrometer (Kratos Analytical Ltd., Manchester, UK) utilizing monochromatic Al-Kα radiation (C1s = 284.6 eV) was employed to investigate the elemental interactions and oxidation states in the synthesized catalysts.

3.4. Catalytic Activity

The volume of hydrogen evolved during the hydrolysis of $NaBH_4$ using the graphitized Bi_2O_3/SiO_2 nanocomposite was quantitatively determined by a water displacement method, as previously described in our published articles [6,10,52]. For each hydrolysis experiment, a control test was carried out to determine the self-hydrolysis behavior of $NaBH_4$ under similar conditions. Typically, 0.5 g of $NaBH_4$ was dissolved in 50 mL of deionized water, previously equilibrated to a specified temperature, and then rapidly transferred into a hydrolysis reactor containing 20 mg of a synthesized catalyst. The hydrolysis system was tightly sealed to facilitate the accurate measurement of the evolved hydrogen gas. The effect of temperature (20, 30, 40, and 50 °C) on hydrolysis reactions was investigated under a constant $NaBH_4$ concentration (0.5 g). On the other hand, the effect of $NaBH_4$ mass (0.3, 0.5, 0.7, and 1.0 mg) on hydrolysis reactions was also investigated under similar conditions.

The hydrogen generation rate (HGR) was calculated at the end of each experiment using equations presented in our previous studies according to the following formula [6,10,52,53]:

$$\mathrm{HGR(mLg^{-1}min^{-1})} = \frac{\mathrm{V(mL)}}{\mathrm{t(min)} \times \mathrm{m(g)}} \quad (1)$$

Here, m represents the catalyst's mass in grams, t the activation time in minutes, and V the total amount of hydrogen released.

The Arrhenius (Equation (2)) and Eyring (Equation (3)) equations were used to determine the activation energy (ΔEa), enthalpy changes of activation ($\Delta H^{\#}$), and entropy change ($\Delta S^{\#}$) [12].

$$\mathrm{Lnk} = \frac{-\mathrm{Ea}}{\mathrm{RT}} + \mathrm{LnA} \quad (2)$$

$$\ln\frac{\mathrm{k}}{\mathrm{T}} = \frac{-\Delta\mathrm{H\#}}{\mathrm{RT}} + \ln\frac{\mathrm{K_B}}{\mathrm{h}} + \frac{\Delta\mathrm{S\#}}{\mathrm{R}} \quad (3)$$

Here, K_B is the Boltzmann constant (1.380649×10^{-23} J·K^{-1}), h is Planck's constant ($6.62607015 \times 10^{-34}$ J·s), and k (min^{-1}) is the particular rate constant connected to pseudo first-order kinetics. T is the absolute temperature in Kelvin, and R is the universal gas constant, which is 8.314 J mol^{-1} K^{-1}.

3.5. Anticancer Activity

The HepG-2 and MCF-7 cells were cultured by incubating for 24 h at 37 °C in RPMI-1640 media, after which $Bi_2O_3/SiO_2/g\text{-}C_3N_4$ was introduced at doses ranging from 3.9 to 500 μg mL^{-1}. Precisely 100 μL of media from each plate was replaced with fresh growth medium, and 10 μL of a 12.0 mmol MTT stock was added. Subsequently, the plates were incubated for 4.0 h at 37 °C in a 5% CO_2 atmosphere. Approximately 85 μL of the medium was replaced with 50 μL of DMS in each plate, which was subsequently re-incubated at 37 °C for an additional 10 min. The optical density was assessed using a microplate reader (Sunrise, TECAN, Inc., Männedorf, Switzerland) at 590 nm, and viability was calculated employing Equation (4).

$$\frac{\mathrm{OD_t}}{\mathrm{OD_c}} \times 100 \quad (4)$$

OD_t and OD_c represent the mean optical densities of treated and untreated cells, respectively. The correlation between viable cells and drug concentration is illustrated to determine the survival rate of each tumor cell line following treatment with the designated substance, and the 50% inhibitory concentration (IC_{50}) was derived from the dose–response curve.

4. Conclusions

Nanoelectronics, magnetite-aided nanocatalysis, and nanomedicine are just a few of the sectors that have shown a significant amount of interest in nanomaterials due to their interesting properties. This article presents the formulation of a 10% Bi_2O_3-10% g-C_3N_4@SiO_2 triple nanohybride via a straightforward process that employs acacia powder as a capping and fuel agent. The X-ray diffraction demonstrated the presence of g-C_3N_4, Bi_2SiO_5, and Bi_2O_3, as well as SiO_5 phases. The transmission electron microscopy (TEM) image reveals tightly packed, virtually spherical nanoparticles with an average size of 9.2 nanometers. During the XPS analysis of $Bi_2O_3/SiO_2/g\text{-}C_3N_4$, peaks were observed that were associated with the elements Bi, Si, O, C, and N. These peaks were observed with binding energies of 30.08, 107.2, 537.71, 290.16, and 402.32 eV, respectively. These results indicate that the developed catalyst is extraordinarily pure. In the field of hydrogen

generation through $NaBH_4$ hydrolysis, the activity of the $Bi_2O_3/SiO_2/g\text{-}C_3N_4$ compound was investigated. Additionally, the anticancer and antiproliferation activity was evaluated against HepG-2 and MCF-7 cells. HGRs of 303, 615, 785, and 1740 mL min^{-1} g^{-1} were observed for graphitized Bi_2O_3/SiO_2 at 20, 30, 40, and 50 degrees Celsius, respectively. This resulted in significant HGR increases of 526, 785, 1786, and 4000 mL min^{-1} g^{-1}, respectively, when $NaBH_4$ dosages of 0.3, 0.5, 0.7, and 1.0 were hydrolyzed at 40 degrees Celsius. In addition, the antiproliferative effect of $SiO_2/g\text{-}C_3N_4/Bi_2SiO_5@Bi_2O_3$ against HepG-2 and MCF-7 cells showed a favorable effect at concentrations of 3.9 and 7.9 µg/mL, with IC50 values of 82.4 and 59.6 µg/mL, respectively. Furthermore, it was observed that the maximal dose of 500 µg/mL of $SiO_2/g\text{-}C_3N_4/Bi_2SiO_5@Bi_2O_3$exhibited a remarkable inhibition of 93.8% in MCF-7 cells. Similarly, the same dose inhibited HepG-2 cells by 91.7%. Given that the cost of $SiO_2/g\text{-}C_3N_4/Bi_2SiO_5@Bi_2O_3$ is significantly lower than that of antitumor medications currently prescribed, it is important to emphasize that these outcomes can be deemed optimal for practical use as antitumor agents.

Author Contributions: Conceptualization, M.K. and B.Y.A., and M.N.G.; methodology, B.Y.A.; validation, formal analysis, and investigation, M.K. and B.Y.A., and M.N.G.; data curation, M.N.G.; writing—original draft preparation, M.K. and B.Y.A., and M.N.G.; writing—review and editing, M.K. and M.N.G. All authors have read and agreed to the published version of the manuscript.

Funding: This work was supported and funded by the Deanship of Scientific Research at Imam Mohammad Ibn Saud Islamic University (IMSIU) (grant number IMSIU-DDRSP2603).

Institutional Review Board Statement: Not applicable.

Informed Consent Statement: Not applicable.

Data Availability Statement: The original contributions presented in this study are included in the article. Further inquiries can be directed to the corresponding authors.

Conflicts of Interest: Authors declare no conflicts of interest.

References

1. Gawande, M.B.; Bonifácio, V.D.B.; Varma, R.S.; Nogueira, I.D.; Bundaleski, N.; Ghumman, C.A.A.; Teodoro, O.M.N.D.; Branco, P.S. Magnetically recyclable magnetite–ceria (Nanocat-Fe-Ce) nanocatalyst—Applications in multicomponent reactions under benign conditions. *Green Chem.* **2013**, *15*, 1226–1231. [CrossRef]
2. Gawande, M.B.; Bonifácio, V.D.B.; Luque, R.; Branco, P.S.; Varma, R.S. Benign by design: Catalyst-free in-water, on-water green chemical methodologies in organic synthesis. *Chem. Soc. Rev.* **2013**, *42*, 5522–5551. [CrossRef] [PubMed]
3. Manna, J.; Roy, B.; Sharma, P. Efficient hydrogen generation from sodium borohydride hydrolysis using silica sulfuric acid catalyst. *J. Power Sources* **2015**, *275*, 727–733. [CrossRef]
4. Mackenzie, J.D.; Bescher, E.P. Chemical Routes in the Synthesis of Nanomaterials Using the Sol–Gel Process. *Acc. Chem. Res.* **2007**, *40*, 810–818. [CrossRef] [PubMed]
5. Tonelli, D.; Scavetta, E.; Gualandi, I. Electrochemical Deposition of Nanomaterials for Electrochemical Sensing. *Sensors* **2019**, *19*, 1186. [CrossRef] [PubMed]
6. Elamin, M.R.; Abdulkhair, B.Y.; Elzupir, A.O. Insight to aspirin sorption behavior on carbon nanotubes from aqueous solution: Thermodynamics, kinetics, influence of functionalization and solution parameters. *Sci. Rep.* **2019**, *9*, 12795. [CrossRef] [PubMed]
7. Bhaskar, M.P.; Nair, S.; Santhanagopalan, D. Cobalt-free CuO catalyst for hydrolytic dehydrogenation of sodium borohydride and ammonia borane. *Int. J. Hydrogen Energy* **2024**, *51*, 551–561. [CrossRef]
8. Goda, M.N.; Abdulkhair, B.Y.; Khairy, M.; Alqarni, L.S.; Alghamdi, M.D.; Ibrahim, T.G.; El-Lateef, H.M.A. Facile solid-state synthesis of $CuO/MgAl_2O_4$ catalysts for sustainable hydrogen generation. *Int. J. Hydrogen Energy* **2026**, *222*, 154257. [CrossRef]
9. Götze, J. Classification, Mineralogy and Industrial Potential of SiO_2 Minerals and Rocks. In *Quartz: Deposits, Mineralogy and Analytics*; Springer: Cham, Switzerland, 2012; pp. 1–27. [CrossRef]
10. Mangold, H.; Rochnia, M. Fumed Silica Produced by Flame Hydrolysis, Process for Its Production and Its Use. US20040253164A1, 16 December 2004.
11. Seo, H.; Kim, D.; Ahn, H.S.; Hwang, S.; Luu, Q.S.; Kim, J.; Lee, S.; Lee, Y. Efficient Conversion Method of Bulk Silicon Powders into Porous Silicon Nanoparticles. *Bull. Korean Chem. Soc.* **2018**, *39*, 1455–1458. [CrossRef]

12. Kuluozturk, Z.N.; Kurtulus, R.; Demir, N.; Kavas, T. Synthesis and Characterization of La_2O_3–BaO–Na_2O–SiO_2–Bi_2O_3 Glass as a Potent Shield Against Ionizing Radiation. *Arab. J. Sci. Eng.* **2024**, *49*, 9923–9936. [CrossRef]
13. Arooj, A.; Tahir, K.; Khan, A.U.; Khan, A.; Jevtovic, V.; El-Zahhar, A.A.; Alghamdi, M.M.; Al-Shehri, H.S.; Saleh, E.A.M.; Asghar, B.H. One-step fabrication of surfactant mediated Pd/SiO_2, A prospect toward therapeutic and photocatalytic applications. *Inorg. Chem. Commun.* **2022**, *142*, 109692. [CrossRef]
14. Nguyen, T.T.; Edalati, K. Efficient photocatalytic hydrogen production on defective and strained black bismuth (III) oxide. *Int. J. Hydrogen Energy* **2024**, *96*, 841–848. [CrossRef]
15. Zhang, L.; Wang, W.; Yang, J.; Chen, Z.; Zhang, W.; Zhou, L.; Liu, S. Sonochemical synthesis of nanocrystallite Bi_2O_3 as a visible-light-driven photocatalyst. *Appl. Catal. A Gen.* **2006**, *308*, 105–110. [CrossRef]
16. Mane, V.; Dake, D.; Raskar, N.; Sonpir, R.; Stathatos, E.; Dole, B. A review on Bi_2O_3 nanomaterial for photocatalytic and antibacterial applications. *Chem. Phys. Impact* **2024**, *8*, 100517. [CrossRef]
17. Singh, K.J.; Kaur, S.; Kaundal, R.S. Comparative study of gamma ray shielding and some properties of PbO–SiO_2–Al_2O_3 and Bi_2O_3–SiO_2–Al_2O_3 glass systems. *Radiat. Phys. Chem.* **2014**, *96*, 153–157. [CrossRef]
18. Ismail, M.M.; Abo-Mosallam, H.A.; Darwish, A.G. Influence of SrO on structural, optical and electrical properties of LiF-MgO-Bi_2O_3-SiO_2 glasses for energy storage applications. *J. Non. Cryst. Solids* **2022**, *590*, 121667. [CrossRef]
19. Khairy, M.; Abdulkhair, B.Y.; Goda, M.N.; Alqarni, L.S.; Ibrahim, T.G.; Nassar, M.Y. Facile synthesis of nanocrystalline Bi_2O_3/SiO_2 catalysts for hydrogen generation via $NaBH_4$ dehydrogenation. *Int. J. Hydrogen Energy* **2025**, *147*, 149991. [CrossRef]
20. Ibrahim, T.G.; Almufarij, R.S.; Abdulkhair, B.Y.; Ramadan, R.S.; Eltoum, M.S.; Elaziz, M.E.A. Thorough Examination of the Solution Conditions and the Use of Carbon Nanoparticles Made from Commercial Mesquite Charcoal as a Successful Sorbent for Water Remediation. *Nanomaterials* **2023**, *13*, 1485. [CrossRef] [PubMed]
21. Foroutan, R.; Peighambardoust, S.J.; Peighambardoust, S.H.; Pateiro, M.; Lorenzo, J.M. Adsorption of Crystal Violet Dye Using Activated Carbon of Lemon Wood and Activated Carbon/Fe_3O_4 Magnetic Nanocomposite from Aqueous Solutions: A Kinetic, Equilibrium and Thermodynamic Study. *Molecules* **2021**, *26*, 2241. [CrossRef] [PubMed]
22. Wu, K.; Chen, D.; Fang, J.; Wu, S.; Yang, F.; Zhu, X.; Fang, Z. One-step synthesis of sulfur and tungstate co-doped porous g-C_3N_4 microrods with remarkably enhanced visible-light photocatalytic performances. *Appl. Surf. Sci.* **2018**, *462*, 991–1001. [CrossRef]
23. Long, B.; Lin, J.; Wang, X. Thermally-induced desulfurization and conversion of guanidine thiocyanate into graphitic carbon nitride catalysts for hydrogen photosynthesis. *J. Mater. Chem. A* **2014**, *2*, 2942–2951. [CrossRef]
24. Wu, P.; Wang, J.; Zhao, J.; Guo, L.; Osterloh, F.E. Structure defects in g-C_3N_4 limit visible light driven hydrogen evolution and photovoltage. *J. Mater. Chem. A* **2014**, *2*, 20338–20344. [CrossRef]
25. Almufarij, R.S.; Abdulkhair, B.Y.; Salih, M. Fast-simplistic fabrication of MoO_3@Al_2O_3-MgO triple nanocomposites for efficient elimination of pharmaceutical contaminants. *Results Chem.* **2024**, *7*, 101281. [CrossRef]
26. Zhang, Y.; Wang, Q.; Chen, Q.; Li, X.; Li, Y.; Kang, M.; Li, Q.; Wang, J. A new boron modified carbon nitride metal-free catalyst for the cycloaddition of CO_2 and bisepoxides. *Appl. Catal. A Gen.* **2024**, *675*, 119615. [CrossRef]
27. Zhou, P.; Yang, Q.; Tang, Y.; Cai, Y. Recent trends in metal-doped carbon nitride-catalyzed heterogeneous light-driven organic transformations. *Nano Trends* **2023**, *4*, 100019. [CrossRef]
28. Elamin, M.R.; Abdulkhair, B.Y.; Elamin, N.Y.; Albadri, A.; Ismail, M.; Bakheit, R.; Taha, K.K.; Modwi, A. Ru@Co_3O_4@g-C_3N_4 as a novel adsorbent for enhanced copper and cadmium abolition. *J. Sci. Adv. Mater. Devices* **2024**, *9*, 100725. [CrossRef]
29. Salih, M.; Ibrahim, T.G.; Ramadan, R.S.; Alarifi, N.; Abdulkhair, B.Y. Fabrication of Spinel Magnesium Aluminate Doped with Divalent-First-Row Transition-Metal Oxides as Efficient Sorbents for Pharmaceutical Contaminants. *Processes* **2025**, *13*, 3095. [CrossRef]
30. Elhadi Abdulkhair, B.Y.; El-Hameed Ibrahim, M.N.A.; Omran, M.K. Nanocomposite of Graphitic C_3N_4, MnO_2, and $MgAl_2O_4$ for Hydrogen Generation. US12365586B1, 22 July 2025. Available online: https://patents.google.com/patent/US12365586B1/en?q=(Nanocomposite+of+graphitic+C3N4%2C+MnO2%2C+and+MgAl2O4+hydrogen+generation)&oq=Nanocomposite+of+graphitic+C3N4%2C+MnO2%2C+and+MgAl2O4+for+hydrogen+generation (accessed on 4 May 2026).
31. Maturi, K.C.; Madeti, S.R.K.; Sinha, S.; Saikia, S.; Srivastava, A.; Haq, I. Revolutionizing bio-hydrogen production: Smart integration of nanotechnology, microbial engineering, and circular waste valorisation. *Bioresour. Bioprocess.* **2026**, *13*, 17. [CrossRef] [PubMed]
32. Blackadar, C.B. Historical review of the causes of cancer. *World J. Clin. Oncol.* **2016**, *7*, 54–86. [CrossRef] [PubMed]
33. Reddy, B.C.; Seenappa, L.; Manjunatha, H.C.; Vidya, Y.S.; Sridhar, K.N.; Kumar, C.M.; Pasha, U.M. Study of antimicrobial applications of Bismuth Oxide. *Mater. Today Proc.* **2022**, *57*, 112–115. [CrossRef]
34. Algethami, F.K.; Elamin, M.R.; Abdulkhair, B.Y.; Al-Zharani, M.; Qarah, N.A.S.; Alghamdi, M.A. Fast fabrication of bismuth oxyiodide/carbon-nanofibers composites for efficient anti-proliferation of liver and breast cancer cells. *Z. Anorg. Allg. Chem.* **2021**, *647*, 1921–1929. [CrossRef]
35. Abdelmonem, E.E.; Khairy, M.; Mohamed, M.M. Innovative Electrocatalytic Water Splitting Utilizing WS_2 and Calcium Silicate Composite for Enhanced Hydrogen Production. *J. Inorg. Organomet. Polym. Mater* **2026**, 1–17. [CrossRef]

36. Bera, K.K.; Chakraborty, M.; Mondal, M.; Banik, S.; Bhattacharya, S.K. Synthesis of α-β Bi_2O_3 heterojunction photocatalyst and evaluation of reaction mechanism for degradation of RhB dye under natural sunlight. *Ceram. Int.* **2020**, *46*, 7667–7680. [CrossRef]
37. Zhou, G.; Huang, Y.; Wei, D.; Fan, Z.; Seo, H.J. Solvothermal synthesis, morphology, and optical properties of Bi_2O_3 and $Bi/Bi_2O_{2.75}$ powders. *J. Nanoparticle Res.* **2020**, *22*, 15. [CrossRef]
38. Yañez-Cruz, M.G.; Villanueva-Ibáñez, M.; Méndez-Arriaga, F.; Lucho-Constantino, C.A.; de los Ángeles Hernández-Pérez, M.; del Rocío Ramírez-Vargas, M.; Flores-González, M.A. Green route synthesis and characterization of β-Bi_2O_3/SiO_2 and β-$Bi_2O_3/Bi_2O_{2.75}/SiO_2$ using *Juglans regia* L. shell aqueous extract and photocatalytic properties for the degradation of RB-5. *J. Anal. Sci. Technol.* **2022**, *13*, 52. [CrossRef]
39. Yang, D.; Fan, T.; Zhou, H.; Ding, J.; Zhang, D. Biogenic Hierarchical TiO_2/SiO_2 Derived from Rice Husk and Enhanced Photocatalytic Properties for Dye Degradation. *PLoS ONE* **2011**, *6*, e24788. [CrossRef] [PubMed]
40. Xia, P.; Zhu, B.; Yu, J.; Cao, S.; Jaroniec, M. Ultra-thin nanosheet assemblies of graphitic carbon nitride for enhanced photocatalytic CO_2 reduction. *J. Mater. Chem. A* **2017**, *5*, 3230–3238. [CrossRef]
41. Wang, R.; Kong, X.; Zhang, W.; Zhu, W.; Huang, L.; Wang, J.; Zhang, X.; Liu, X.; Hu, N.; Suo, Y.; et al. Mechanism insight into rapid photocatalytic disinfection of Salmonella based on vanadate QDs-interspersed g-C_3N_4 heterostructures. *Appl. Catal. B Environ.* **2018**, *225*, 228–237. [CrossRef]
42. Yu, J.; Wang, S.; Cheng, B.; Lin, Z.; Huang, F. Noble metal-free $Ni(OH)_2$–g-C_3N_4 composite photocatalyst with enhanced visible-light photocatalytic H2-production activity. *Catal. Sci. Technol.* **2013**, *3*, 1782–1789. [CrossRef]
43. Wang, W.; Zhang, H.; Zhang, S.; Liu, Y.; Wang, G.; Sun, C.; Zhao, H. Potassium-Ion-Assisted Regeneration of Active Cyano Groups in Carbon Nitride Nanoribbons: Visible-Light-Driven Photocatalytic Nitrogen Reduction. *Angew. Chem.-Int. Ed.* **2019**, *58*, 16644–16650. [CrossRef] [PubMed]
44. Tang, M.; Ao, Y.; Wang, C.; Wang, P. Facile synthesis of dual Z-scheme g-C_3N_4/Ag_3PO_4/AgI composite photocatalysts with enhanced performance for the degradation of a typical neonicotinoid pesticide. *Appl. Catal. B Environ. Energy* **2020**, *268*, 118395. [CrossRef]
45. Liu, W.; Shen, J.; Yang, X.; Liu, Q.; Tang, H. Dual Z-scheme g-$C_3N_4/Ag_3PO_4/Ag_2MoO_4$ ternary composite photocatalyst for solar oxygen evolution from water splitting. *Appl. Surf. Sci.* **2018**, *456*, 369–378. [CrossRef]
46. Wang, X.; Cheng, J.; Yu, H.; Yu, J. A facile hydrothermal synthesis of carbon dots modified g-C_3N_4 for enhanced photocatalytic H2-evolution performance. *Dalt. Trans.* **2017**, *46*, 6417–6424. [CrossRef] [PubMed]
47. Jo, W.K.; Selvam, N.C.S. Z-scheme CdS/g-C_3N_4 composites with RGO as an electron mediator for efficient photocatalytic H_2 production and pollutant degradation. *Chem. Eng. J.* **2017**, *317*, 913–924. [CrossRef]
48. Goda, M.N.; Alqarni, L.S.; Khairy, M.; Abou-Krisha, M.M.; Abdulkhair, B.Y.; Abdelrahman, E.A.; Mahmoud, G.A.E. Hydrothermal Synthesis of Microporous $CuWO_4$ for Hydrogen Generation and Antibacterial Activity. *J. Inorg. Organomet. Polym. Mater.* **2025**, *35*, 7218–7232. [CrossRef]
49. Santen, R.A.V.; Neurock, M.; Shetty, S.G. Reactivity Theory of Transition-Metal Surfaces: A Brønsted−Evans−Polanyi Linear Activation Energy−Free-Energy Analysis. *Chem. Rev.* **2009**, *110*, 2005–2048. [CrossRef] [PubMed]
50. Wei, Z.; Li, Y.; Cooks, R.G.; Yan, X. Accelerated reaction kinetics in microdroplets: Overview and recent developments. *Annu. Rev. Phys. Chem.* **2020**, *71*, 31–51. [CrossRef] [PubMed]
51. Wu, J.; Jia, X.; Wang, M.; Yao, X.; Zhong, L.; Pan, W.-P. Synergy-Driven Enhancement of Sodium Borohydride Hydrolysis over a One-Pot Synthesized Co-Ni Bimetallic MOF. *SSRN* **2026**. [CrossRef]
52. Goda, M.N.; Alqarni, L.S.; Khairy, M.; Abdulkhair, B.Y.; Mahmoud, G.A.E. Metal–Organic Framework (MOF)-Derived Mn_2O_3@C for Sustainable Hydrogen Generation and Antibacterial Efficacy Against Human Pathogenic Bacteria. *Appl. Organomet. Chem.* **2025**, *39*, e70326. [CrossRef]
53. Chen, Y.; Jin, H. Fabrication of amorphous Co–Cr–B and catalytic sodium borohydride hydrolysis for hydrogen generation. *J. Mater. Res.* **2020**, *35*, 281–288. [CrossRef]
54. Beheshti, A.K.; Rezaei, M.; Alavi, S.M.; Akbari, E.; Varbar, M. Cobalt nanoparticle synthesis through the mechanochemical and chemical reduction method as a highly active and reusable catalyst for H_2 production via sodium borohydride hydrolysis process. *Int. J. Hydrogen Energy* **2024**, *51*, 661–670. [CrossRef]
55. Kıpçak, İ.; Kalpazan, E. Preparation of CoB catalysts supported on raw and Na-exchanged bentonite clays and their application in hydrogen generation from the hydrolysis of $NaBH_4$. *Int. J. Hydrogen Energy* **2020**, *45*, 26434–26444. [CrossRef]
56. Said, M.I.; Goda, M.N. Potentially less hazardous hydrogen production: A green catalytic approach using copper aspartate MOF for $NaBH_4$ hydrolysis. *Int. J. Hydrogen Energy* **2025**, *179*, 151669. [CrossRef]
57. Makiabadi, M.; Shamspur, T.; Mostafavi, A. Performance improvement of oxygen on the carbon substrate surface for dispersion of cobalt nanoparticles and its effect on hydrogen generation rate via $NaBH_4$ hydrolysis. *Int. J. Hydrogen Energy* **2020**, *45*, 1706–1718. [CrossRef]
58. Wu, C.; Guo, J.; Zhang, J.; Zhao, Y.; Tian, J.; Isimjan, T.T.; Yang, X. Palladium nanoclusters decorated partially decomposed porous ZIF-67 polyhedron with ultrahigh catalytic activity and stability on hydrogen generation. *Renew. Energy* **2019**, *136*, 1064–1070. [CrossRef]

59. Liu, Z.; Guo, B.; Chan, S.H.; Tang, E.H.; Hong, L. Pt and Ru dispersed on $LiCoO_2$ for hydrogen generation from sodium borohydride solutions. *J. Power Sources* **2008**, *176*, 306–311. [CrossRef]
60. Liang, Z.; Li, Q.; Li, F.; Zhao, S.; Xia, X. Hydrogen generation from hydrolysis of $NaBH_4$ based on high stable NiB/$NiFe_2O_4$ catalyst. *Int. J. Hydrogen Energy* **2017**, *42*, 3971–3980. [CrossRef]
61. Liu, C.H.; Chen, B.H.; Hsueh, C.L.; Ku, J.R.; Tsau, F.; Hwang, K.J. Preparation of magnetic cobalt-based catalyst for hydrogen generation from alkaline $NaBH_4$ solution. *Appl. Catal. B Environ.* **2009**, *91*, 368–379. [CrossRef]
62. Yu, H.; Tshimanga, M.A.; Tshimanga, T.L.W.; Gao, M. Investigation of CoB/SBA-15 Catalyst for Efficient Hydrogen Generation via Sodium Borohydride Hydrolysis. *ChemPhysChem* **2025**, *26*, e202401104. [CrossRef] [PubMed]
63. Li, Q.; Yang, W.; Li, F.; Cui, A.; Hong, J. Preparation of CoB/ZIF-8 supported catalyst by single step reduction and its activity in hydrogen production. *Int. J. Hydrogen Energy* **2018**, *43*, 271–282. [CrossRef]
64. Didehban, A.; Zabihi, M.; Shahrouzi, J.R. Experimental studies on the catalytic behavior of alloy and core-shell supported Co-Ni bimetallic nano-catalysts for hydrogen generation by hydrolysis of sodium borohydride. *Int. J. Hydrogen Energy* **2018**, *43*, 20645–20660. [CrossRef]
65. Didehban, A.; Zabihi, M.; Babajani, N. Preparation of the efficient nano-bimetallic cobalt-nickel catalysts supported on the various magnetic substrates for hydrogen generation from hydrolysis of sodium borohydride in alkaline solutions. *Polyhedron* **2020**, *180*, 114405. [CrossRef]
66. Akti, F. Hydrogen generation from hydrolysis of sodium borohydride by silica xerogel supported cobalt catalysts: Positive roles of amine modification and calcination treatment. *Fuel* **2021**, *303*, 121326. [CrossRef]
67. Demirci, S.; Yildiz, M.; Inger, E.; Sahiner, N. Synthesis of cobalt-doped catalyst for $NaBH_4$ hydrolysis using eggshell biowaste. *Int. J. Hydrogen Energy* **2023**, *48*, 28018–28033. [CrossRef]
68. Ye, W.; Zhang, H.; Xu, D.; Ma, L.; Yi, B. Hydrogen generation utilizing alkaline sodium borohydride solution and supported cobalt catalyst. *J. Power Sources* **2007**, *164*, 544–548. [CrossRef]
69. Aman, D.; Alkahlawy, A.A.; Zaki, T. Hydrolysis of $NaBH_4$ using ZVI/$Fe_2(MoO_4)_3$ nanocatalyst. *Int. J. Hydrogen Energy* **2018**, *43*, 18289–18295. [CrossRef]
70. Lee, J.K.; Ann, H.H.; Yi, Y.; Lee, K.W.; Uhm, S.; Lee, J. A stable Ni–B catalyst in hydrogen generation via $NaBH_4$ hydrolysis. *Catal. Commun.* **2011**, *16*, 120–123. [CrossRef]
71. Zhang, X.; Sun, X.; Xu, D.; Tao, X.; Dai, P.; Guo, Q.; Liu, X. Synthesis of MOF-derived Co@C composites and application for efficient hydrolysis of sodium borohydride. *Appl. Surf. Sci.* **2019**, *469*, 764–769. [CrossRef]
72. Abu-Zied, B.M.; Alamry, K.A. Green synthesis of 3D hierarchical nanostructured Co_3O_4/carbon catalysts for the application in sodium borohydride hydrolysis. *J. Alloys Compd.* **2019**, *798*, 820–831. [CrossRef]
73. Narasimharao, K.; Abu-Zied, B.M.; Alfaifi, S.Y. Cobalt oxide supported multi wall carbon nanotube catalysts for hydrogen production via sodium borohydride hydrolysis. *Int. J. Hydrogen Energy* **2020**, *46*, 6404–6418. [CrossRef]
74. Andrieux, J.; Demirci, U.B.; Miele, P. Langmuir–Hinshelwood kinetic model to capture the cobalt nanoparticles-catalyzed hydrolysis of sodium borohydride over a wide temperature range. *Catal. Today* **2011**, *170*, 13–19. [CrossRef]
75. Yang, C.C.; Chen, M.S.; Chen, Y.W. Hydrogen generation by hydrolysis of sodium borohydride on CoB/SiO_2 catalyst. *Int. J. Hydrogen Energy* **2011**, *36*, 1418–1423. [CrossRef]
76. Ahamed, M.; Akhtar, M.J.; Khan, M.A.M.; Alrokayan, S.A.; Alhadlaq, H.A. Oxidative stress mediated cytotoxicity and apoptosis response of bismuth oxide (Bi_2O_3) nanoparticles in human breast cancer (MCF-7) cells. *Chemosphere* **2019**, *216*, 823–831. [CrossRef] [PubMed]
77. Peng, L.; Li, Z.W.; Zheng, R.R.; Yu, H.; Dong, X.T. Preparation and characterization of mesoporous g-C_3N_4/SiO_2 material with enhanced photocatalytic activity. *J. Mater. Res.* **2019**, *34*, 1785–1794. [CrossRef]
78. Freire, T.M.; Sant'Anna, C.; Yoshihara, N.; Hu, R.; Qu, J.; Alencar, L.M.R.; Da Silva De Barros, A.O.; Helal-Neto, E.; Fernandes, L.R.; Simoes, R.L.; et al. Biomedical application of graphitic carbon nitrides: Tissue deposition in vivo, induction of reactive oxygen species (ROS) and cell viability in tumor cells. *Nanotechnology* **2021**, *324*, 35301. [CrossRef] [PubMed]
79. Alamer, A.; Ali, D.; Alarifi, S.; Alkahtane, A.; AL-Zharani, M.; Abdel-Daim, M.M.; Albasher, G.; Almeer, R.; Al-Sultan, N.K.; Almalik, A.; et al. Bismuth oxide nanoparticles induce oxidative stress and apoptosis in human breast cancer cells. *Environ. Sci. Pollut. Res.* **2020**, *28*, 7379–7389. [CrossRef] [PubMed]
80. Lateef, R.; Ahmad, I.; Mahdi, A.A.; Lohia, N.; Alhadlaq, H.A.; Akhtar, M.J.; Ahamed, M. Toxic Effects of Synthesized Bismuth Oxide/Reduced Graphene Oxide (Bi_2O_3/RGO) Nanocomposites in Two Distinct Mammalian Cell Lines: Role Oxidative Stress and Apoptosis. *Int. J. Nanomed.* **2024**, *19*, 12655–12674. [CrossRef] [PubMed]

Disclaimer/Publisher's Note: The statements, opinions and data contained in all publications are solely those of the individual author(s) and contributor(s) and not of MDPI and/or the editor(s). MDPI and/or the editor(s) disclaim responsibility for any injury to people or property resulting from any ideas, methods, instructions or products referred to in the content.